Available online at www.sciencedirect.com
ScienceDirect
International Journal of Heat and Fluid Flow 27 (2006) 768–776
International Journal of HEAT AND FLUID FLOW
www.elsevier.com/locate/ijhff

The pressure–velocity correlation in oscillatory turbulent flow between a pair of bluff bodies

Shinnosuke Obi *, Norihiko Tokai

Department of Mechanical Engineering, Keio University, Hiyoshi 3-14-1, Kohoku-ku, Yokohama 223-8522, Japan

Received 29 October 2005; received in revised form 23 January 2006; accepted 4 March 2006
Available online 15 June 2006

Abstract

Turbulent flow measurements were conducted between two bluff bodies set in uniform flow in tandem arrangement. The velocity field obtained with PIV was averaged with respect to either time or phase of periodic pressure oscillation induced by vortex shedding from the bluff body, i.e., Reynolds decomposition or three-level decomposition. The Reynolds stresses caused by periodic fluid motion was found excessively large compared with those related to turbulent fluctuations in the entire flow field in observation. The PIV data were used to solve the discrete Poisson equation of instantaneous pressure. The effect of organized vortex motion caused strong correlations between velocity and pressure gradient when observed from the framework of the Reynolds averaging.

Keywords: Turbulent wake; PIV; Reynolds stress; Pressure–velocity correlation; URANS; Three-level decomposition

1. Introduction

Turbulence models based on the Reynolds-averaged Navier–Stokes (RANS) approach often fail to predict flows associated with massive separation, in contrast to LES which can correctly capture large-scale turbulent fluid motion typically found in such flows. It is generally recognized that the poor performance of the RANS models is due to the shortcomings of the statistical approach itself in representing the coherent structure in turbulence. On the other hand, the development of conventional RANS models have relied upon the knowledge of simple shear flows in nearly equilibrium state; hence it is likely that the turbulent transport process, which is relatively important in non-equilibrium flows, is not correctly incorporated into the existing models. In particular, the treatment of *pressure diffusion transport*, which is strong in free shear flows, is still far below a satisfactory level, partly because of the relatively few experimental information on the pressure–velocity correlation. The knowledge about such processes in flows in an out-of-equilibrium state is desired for the development of RANS-based turbulence models.

The turbulent wake of a bluff body put in a uniform flow is a typical example of a problem where RANS-based models exhibit their disadvantage. The length of the wake calculated by RANS models is usually too long compared to experiment and/or LES (e.g., Bosch and Rodi, 1998). This is usually attributed to the vortices shed from the body; hence the application of unsteady RANS (URANS) has become attractive as an alternative to LES (Iaccarino et al., 2003). The theoretical basis for URANS is, however, not firm enough to make this approach a standard tool for engineering design. Detailed discussions based on experimental data are desired.

Turbulent flows associated with periodic motion have often served as attractive topics for experiments in the past. The three-level decomposition technique (Hussain and Reynolds, 1970) has been used as a standard tool to

* Corresponding author. Tel.: +81 45 566 1499; fax: +81 45 566 1495.
E-mail address: obsn@mech.keio.ac.jp (S. Obi).

0142-727X/$ - see front matter © 2006 Elsevier Inc. All rights reserved.
doi:10.1016/j.ijheatfluidflow.2006.03.021

analyze the interaction between periodic motion and turbulence, though its application in experiments is slightly different according to the types of oscillation. From an experimental point of view, the flows under external periodic forcing (e.g., Yoshioka et al., 2001a,b) are convenient for phase-averaging because the oscillation frequency is known. On the other hand, flows comprising natural vortex shedding as represented by the wake of a bluff body require certain treatment for acquisition of meaningful data (Lyn and Rodi, 1994). In any case, the separation of oscillatory motion from turbulent fluctuation is of primary importance for the discussion of organized vortex structure in turbulent flows.

The present study considers the flows associated with natural vortex shedding at nearly constant frequency. Such problems have been considered by Lyn and Rodi (1994) as well as Lyn et al. (1995). The interest in the present study is to analyze the suitability of URANS approach to this kind of flow. The three-level decomposition is applied to separate organized, oscillatory fluid motion from turbulent fluctuation, so that the influence of the shed vortex becomes evident. Furthermore, the instantaneous pressure field is estimated from the velocity data obtained with PIV, so that the effects of the oscillatory motion can be considered in terms of pressure-related statistics. The principle of the pressure field evaluation is introduced in the next section together with its assessment using numerical simulation. Following the presentation of the velocity field, discussions are made on possible requirements for the RANS approach to handle this kind of flow.

2. Principle of the pressure field evaluation

2.1. Basic equations

The Poisson equation for pressure is derived from the divergence of Navier–Stokes equation. Applying the continuity equation, one obtains the following expression:

$$\frac{\partial^2 \hat{p}}{\partial x_i^2} = -\rho \frac{\partial \hat{u}_i}{\partial x_j} \frac{\partial \hat{u}_j}{\partial x_i}, \tag{1}$$

where $\hat{p}$ and $\hat{u}$ denote instantaneous pressure and velocity, respectively. Note that the unsteady term disappears due to continuity. This equation is solved for the instantaneous pressure $\hat{p}$ for the known velocity field appearing on the right-hand-side under appropriate boundary conditions. When the flow field in consideration is fairly homogeneous in one direction, the two-dimensional approximation can be made. Assuming the fluid motion and its spatial derivative in z-direction are negligible, Eq. (1) may be approximated as

$$\frac{\partial^2 \hat{p}}{\partial x^2} + \frac{\partial^2 \hat{p}}{\partial y^2} \simeq 2\rho \left(\frac{\partial \hat{u}}{\partial x} \frac{\partial \hat{v}}{\partial y} - \frac{\partial \hat{u}}{\partial y} \frac{\partial \hat{v}}{\partial x} \right). \tag{2}$$

The terms on the right-hand-side are available from conventional PIV measurement, hence Eq. (2) can be solved under suitable boundary conditions as discussed below.

2.2. Boundary conditions

Because of the elliptic nature of the Poisson equation, boundary conditions are required for all boundaries surrounding the region of interest. To specify the Neumann condition, the pressure gradient normal to the boundaries was estimated using of Euler's equation of fluid motion

$$\frac{\partial \hat{p}}{\partial n} = -\left(\frac{\partial \rho \hat{u}_n}{\partial t} + \hat{u}_n \frac{\partial \rho \hat{u}_n}{\partial n} + \hat{u}_s \frac{\partial \rho \hat{u}_n}{\partial s} \right), \tag{3}$$

with u_n and u_s being the velocity components in n- and s-directions, respectively, where n is taken normal to the boundary. As will be described below, time resolution of available PIV is too low to estimate the unsteady term, so it is omitted for simplicity. The velocity data obtained by PIV is supplied to Eq. (3), which is then used to specify the boundary condition of Eq. (2). The possible errors due to the neglect of the unsteady terms and the two-dimensional approximation will be discussed below.

2.2.1. Numerical method

The numerical solution of Eq. (3) was obtained by means of a finite-volume method. In the computation domain, control volumes (CV) were placed at grid points of even interval. Denoting the variable at the center of each CV by subscript P and those surrounding it by E, W, N, and S, a discrete equation was derived from Eq. (2) as

$$\hat{p}_P = \frac{1}{4}(\hat{p}_E + \hat{p}_W + \hat{p}_N + \hat{p}_S) - S, \tag{4}$$

with S being the source term of the right-hand-side of Eq. (2):

$$S = 2\rho \left(\frac{\partial \hat{u}}{\partial x} \frac{\partial \hat{v}}{\partial y} - \frac{\partial \hat{u}}{\partial y} \frac{\partial \hat{v}}{\partial x} \right) \Delta x \Delta y.$$

The contents of S were calculated by differentiating the velocity data obtained by PIV measurement. The matrix of the calculation grid was 56×60 in x- and y-directions. The iterative line-by-line method was adopted to solve Eq. (4).

2.3. Assessment using numerical simulation

The above-mentioned method of the pressure field evaluation has two approximations, i.e., the neglect of three-dimensional fluid motion and the steady state simplification of the boundary condition. These issues were addressed by using the data set of numerical simulation for turbulent wake of a rectangular cylinder in a uniform flow. The computation was performed in the region covering

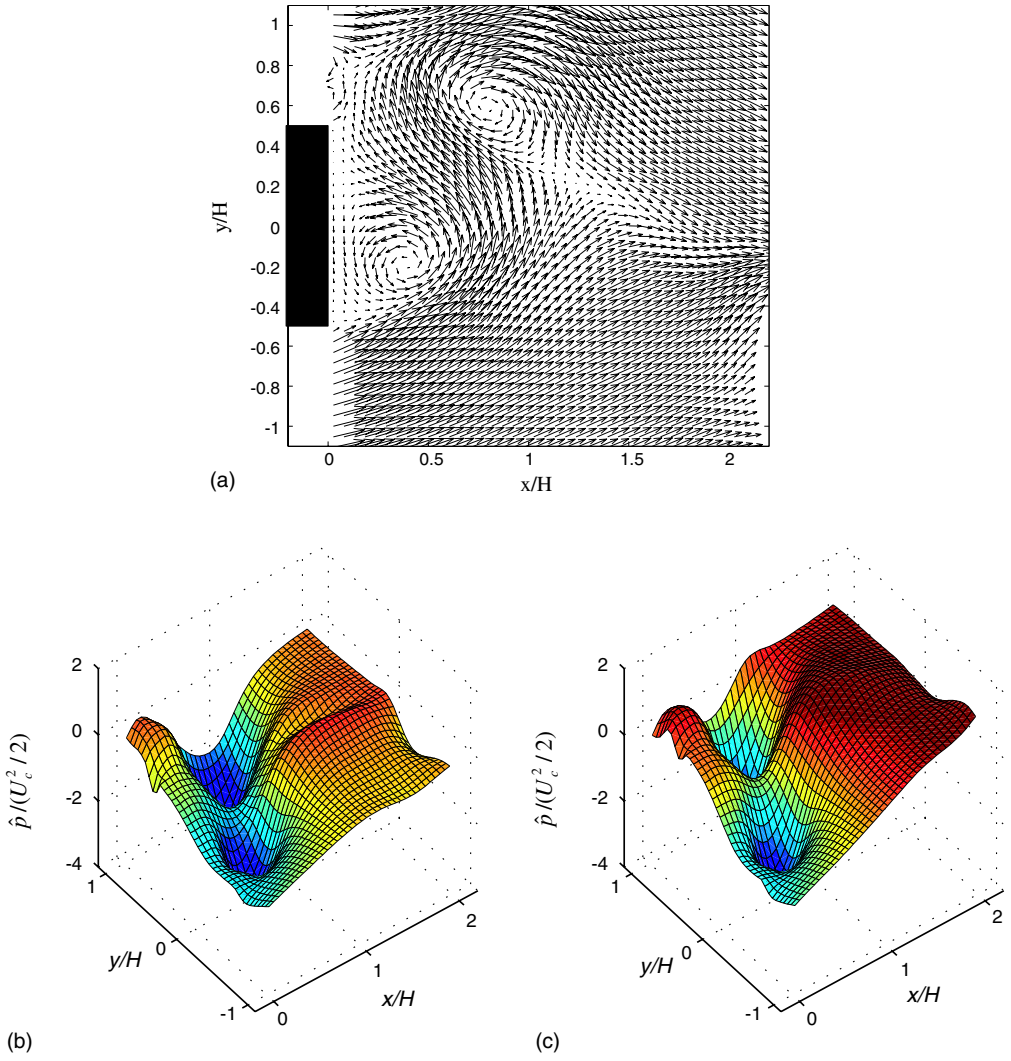

Fig. 1. Comparison between numerical simulation and the present method: (a) instantaneous velocity field, (b) instantaneous pressure (simulation) and (c) instantaneous pressure (present method).

$25H \times 5H \times 10H$ in x-, y- and z-directions, with H being the length of the rectangular cylinder cross section. The number of control volumes were $142 \times 130 \times 26$, where a second-order finite-volume method was applied. Based on H and the uniform mean velocity, U_c, the Reynolds number was $Re = 1100$. Statistics presented below were calculated averaging over 2400 samples of velocity–pressure fields. Fig. 1 shows instantaneous velocity vectors and pressure field of the numerical simulation, comparing the pressure field evaluated by present method. Eq. (3) without the unsteady term was applied as boundary condition except for the wall of the cylinder where zero pressure gradient $\partial\hat{p}/\partial x = 0$ was applied.

In the simulated pressure field, Fig. 1(b), it is observed that there are two local minima at points $(x/H, y/H) = (0.8, 0.6)$ and $(0.4, -0.2)$. A comparison of these pressure distributions with the instantaneous velocity field shown in Fig. 1(a) reveals that these pressure minima are well correlated with the location of vortices. In the pressure field evaluated by the Poisson equation, Fig. 1(c), two local minima at the same locations are observed. The result indicates that the pressure field behind a cylinder is well correlated with the two-dimensional velocity field. This supports the assumption that the two-dimensional approximation in the present method is acceptable.

Next, the uncertainty due to the approximated boundary condition was examined by referring the correlation between pressure field evaluated by the Poisson equation and that of the simulation. Fig. 2 shows the correlation coefficient of the simulated pressure and the pressure deduced from the present method (R) at various $x-$ locations in the wake. R ranges from 0.6 to 0.8 at various streamwise locations along the centerline of the bluff body. However, it is rather low near the boundaries. These small values of R can be attributed to the neglect of the unsteady terms in Eq. (3) to specify the boundary conditions. Although the discrepancy is somewhat high near the boundaries, the instantaneous pressure can be evaluated

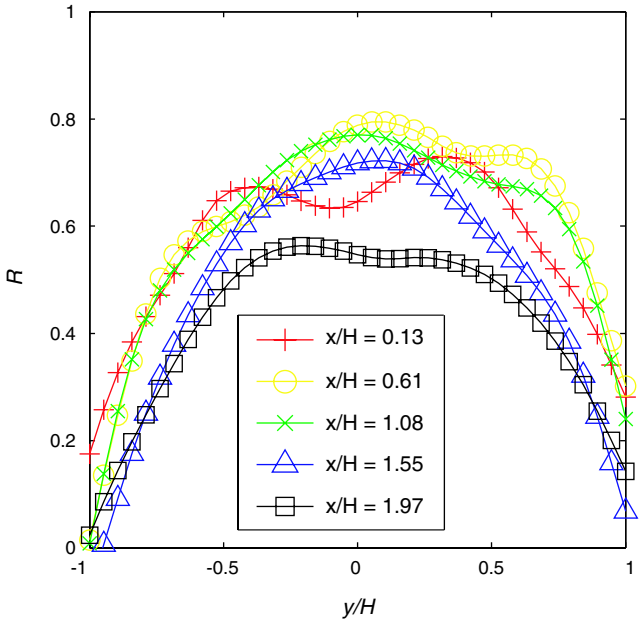

Fig. 2. Correlation of pressure field between the simulation and the present method.

by the present method with satisfactory accuracy in most of the domain.

3. Experiment

3.1. Test section

The flow around a pair of bluff bodies as shown in Fig. 3, representing a recent multiple bridge construction (e.g., Vezza and Taylor, 2003), was considered. The issue here was the wind load exerted on the body which was located in the wake of another, i.e., the vortex shed from the upstream body impinges on the second body and causes a fluctuating force with significant amplitude. To understand the flow dynamics in such a configuration, the present study focuses on the region between the two bodies, as shown by a box marked with broken lines.

The measurements were performed in a closed loop circuit of water. The cross section of the working section was rectangular (0.13 m × 0.3 m), and the bluff bodies were set 0.75 m from the entrance of the working section whose total length was 1.9 m. The dimension of the bluff body H was 30 mm, yielding a blockage ratio of 0.1 and an aspect ratio of 4.3.

The velocity of the oncoming uniform flow U_c was varied through the range 0.1 m/s $\leqslant U_c \leqslant$ 0.3 m/s. The Reynolds number based on H and U_c was $3000 \leqslant Re \leqslant 9000$. The free stream turbulence was measured to be below 1%. The mean flow was observed to be homogeneous in the spanwise direction; hence the velocity measurements were undertaken at the center of the span.

3.2. PIV measurements

A PIV system comprising an 8-bit digital camera with 1008 × 1018 pixels (REDLAKE, ES1.0) and a ND:YAG Laser with 30 mJ output power (New Wave, Solo PIV) was used. The thickness of the light sheet was approximately 1 mm. White Nylon 12 particles, 90 μm in mean diameter and with a specific gravity of 1.02 were used as a tracer. A pair of successive images were acquired with a frame grabber (National Instruments, PCI-1422) and sent to a 32 bit PC at a interval of $\Delta t = 2.5$ ms controlled by an external trigger (National Instruments, PCI-6602). The resulting conversion factor to yield physical length was 0.055 mm/pixel. The velocity vectors were evaluated by direct correlation method using an interrogation area of 32 × 32 pixels with 50% overlap in both directions, and erroneous vectors were eliminated by applying a spatial filter. The percentage of the erroneous vectors per image was approximately 5%. In order to assure the independence of each velocity data for statistic processing, the acquisition rate was determined to be 1 Hz which was on the same order of the vortex shedding frequency.

3.3. Phase detection

The phase-averaging of the velocity field was conducted with reference to pressure fluctuations on the surface of the upstream body. The instrumentation illustrated in Fig. 4 was used to synchronize the pressure and PIV measurements. The reference pressure was measured on the round surface of the body, cf. Fig. 5(a); this location was selected because strong velocity fluctuations were observed in preliminary measurements using LDV (not shown). The static pressure was sensed at a round hole of 1.0 mm in diameter

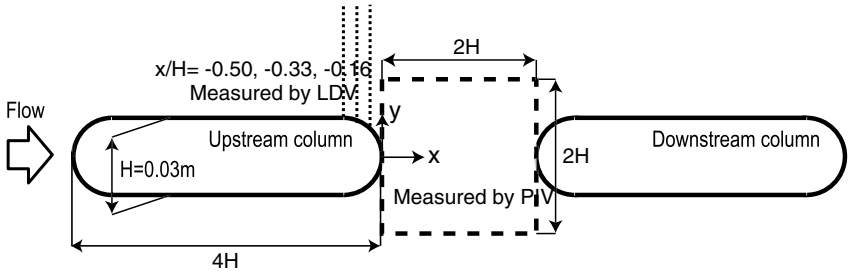

Fig. 3. Measurement area.

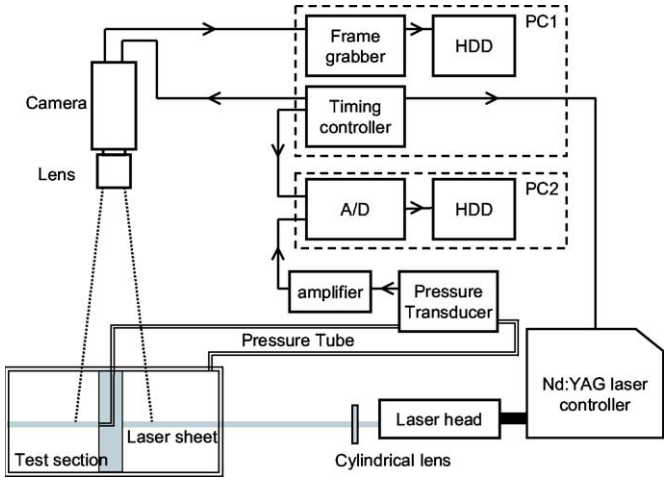

Fig. 4. Instrumentation.

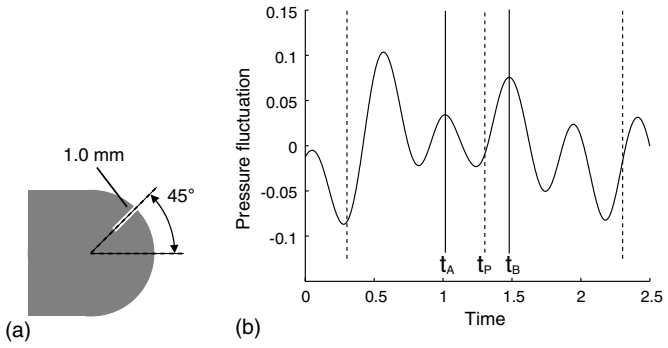

Fig. 5. Principle of the phase-averaging with respect to the pressure on the surface of the body: (a) location of the pressure measurement and (b) definition of t_A, t_B to detect phase.

and evaluated with a precision transducer (Validyne, DP103) in differential mode with respect to the pressure measured on the wall of the water channel at a position away from the obstacle, $(x/H, y/H) = (-8.5, -2.8)$. The analogue electronic signal was amplified and digitized with a 16 bit A/D converter (National Instruments, PCI-6040E) at a rate of 400 Hz. The pulse signal for controlling the PIV was recorded simultaneously with the pressure signal for detection of phase as described later. Since the frequency of vortex shedding was evaluated to be $f_s = 2.1$ Hz by preliminary experiments, a low-pass filter at 4 Hz was applied to the pressure signal to prevent aliasing distortion of the signal.

The phase with respect to the dominant frequency of the pressure fluctuations was evaluated according to the practice proposed by Lyn and Rodi (1994). As illustrated in Fig. 5(b), the phase angle ϕ was detected as follows: A pair of successive peaks were sought in the low-pass filtered fluctuating pressure signal and the instants at which the pressure reaches maxima were specified as t_A and t_B, respectively. The instant at which the velocity data was stored, t_P, was used to determine the phase according to

$$\phi = 2\pi \frac{t_P - t_A}{t_B - t_A}. \quad (5)$$

Note that the time t_P was the midpoint of the instants at which two successive images were acquired. This procedure was necessary to allow a slight change in the frequency of regular vortex shedding. The spectra of the filtered fluctuating pressure, shown in Fig. 6(a), indicates the dominant frequency of $St = f_s H/U \sim 0.21$, though, at the same time, a significant amount of the fluctuation exists at a lower frequency than f_s. These slow fluctuations resulted in the modulation of vortex shedding frequency, as illustrated by the probability density function of the characteristic period $(t_B - t_A)$, in Fig. 6(b).

The velocity data were separated into 20 groups according to ϕ, so that each group corresponded to a discrete phase angle of $\Delta\phi = 0.1\pi$, the average over each group providing a discrete variation over $0 \leqslant \phi < 2\pi$. When the characteristic period $(t_B - t_A)$ did not satisfy the condition $0.5 < f_s(t_B - t_A) < 1.5$, the pressure fluctuation was considered to be out of phase, and the corresponding velocity data were rejected. As a consequence, the valid data were approximately 82.2% of whole sample of 8000 points, resulting in about 330 samples for every phase angle band. It should be noted, however, that the all data, i.e., 8000 points, were used for time-averaging.

4. Results

4.1. Effect of Reynolds number

The length of the time-averaged recirculation zone is first examined because it is known to reflect the gross influence of the variation of Reynolds number on flow around a bluff body (Zdravkovich, 1997). Fig. 7 presents the length

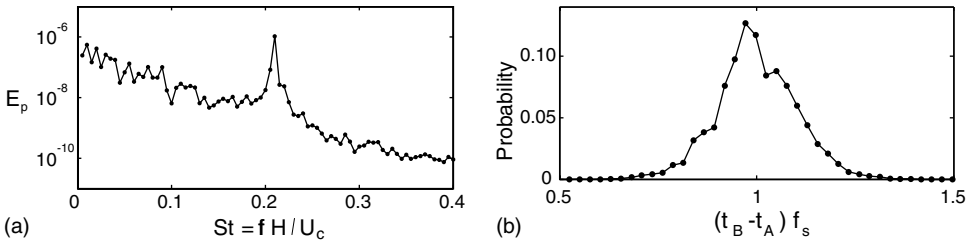

Fig. 6. Characteristics of pressure fluctuation on the surface of the body: (a) spectrum of filtered pressure fluctuation and (b) PDF of characteristic period.

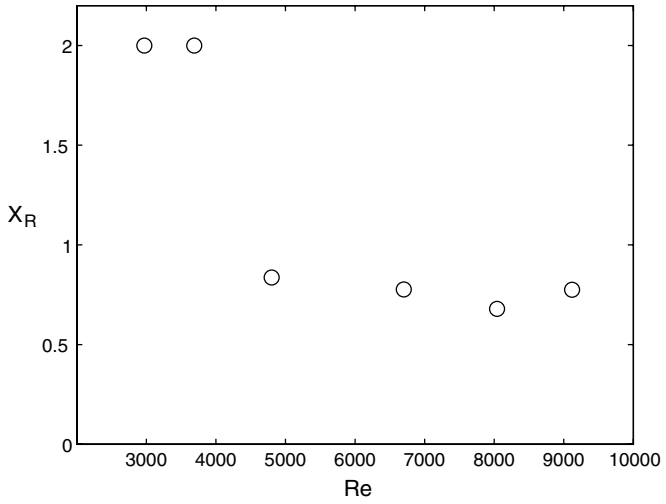

Fig. 7. Length of recirculation zone behind the body in upstream side.

of the recirculation zone x_R, determined as the streamwise coordinate on the centerline at which the streamwise mean velocity changes its sign, as a function of Reynolds number. Note that x_R is normalized by H. It is indicated that the recirculation zone reaches the second body at lower Reynolds number, $Re \leqslant 4000$, while x_R stays nearly constant for $4000 \leqslant Re \leqslant 9000$, yielding $x_R = 0.8$. This is in good accordance with a separate experiment conducted in a wind tunnel (Kuroda et al., 2003). The results shown in the subsequent sections are obtained at $Re = 9000$ so that the influence of Reynolds number is minimized.

4.2. Streamlines

The phase-averaging procedure described in the preceding section enables the instantaneous velocity to be decomposed into the periodically varying part and fluctuations around it:

$$\hat{u}_i = \langle u_i \rangle + u_i', \tag{6}$$

where the velocity in bracket, u_i, is phase-averaged velocity that varies with time or with phase ϕ. Fig. 8(a) shows the streamline pattern obtained by smoothly connecting the time-averaged velocity vectors. A pair of recirculation zones is observed behind the upstream body. On the other hand, the phase-averaged streamlines obtained from u_i, shown in Fig. 8(b) and (c), demonstrate the evolution of a wavy pattern as a consequence of the shed vortex. The phase $\phi = 0$ corresponds to the instant at which the fluctuating pressure detected on the body surface reaches the maximum. In reference to the location of the pressure measurement, cf. Fig. 5(a), it is recognized that a vortex is about to leave the opposite side of the body.

4.3. Reynolds stresses

The instantaneous velocity $\hat{u}_i$ may also be expressed by a sum of mean velocity U_i, periodic component $\tilde{u}_i$, and turbulent component u_i' as

$$\hat{u}_i = U_i + \tilde{u}_i + u_i'. \tag{7}$$

Subtraction of the mean velocity U_i from $\langle u_i \rangle$ introduced in Eq. (6) provides the periodic velocity fluctuation $\tilde{u}_i$, so that the periodic and turbulent velocity fluctuation are distinguished from each other.

The distribution of streamwise normal component of Reynolds stress $\overline{u^2}$ is shown in Fig. 9, comparing the Reynolds stresses calculated from the time average of whole sample to those calculated from the periodic velocity fluctuation and turbulent components. The $\overline{u^2}$-component shows two separate regions of high intensity, located along the shear layer separated from the upstream body. It reaches the maximum at $x/H \approx 0.5$, and gradually decreases downstream. Comparing the turbulent and periodic parts, one can see that the turbulent part is concentrated in the near-wake region where a pair of steep peaks is observed, while the periodic part develops in the middle of the observed field, reflecting the fluctuation due to shed vortices.

The shear stress component $\overline{uv}$ shown in Fig. 10 resembles that of the $\overline{u^2}$ component in the sense that there are two separate peaks, positive and negative, along the separated shear layer. The evolution of the periodic part, Fig. 10(c), occurs in the middle of the two bodies, in accordance with the observation of $\overline{\tilde{u}^2}$ in Fig. 9(c).

In contrast to these two components, the $\overline{v^2}$-component shown in Fig. 11 indicates qualitatively different tendency; a broad peak is located in the center of the wake and a notable peak is observed right in front of the downstream body. The decomposition of this quantity into turbulent

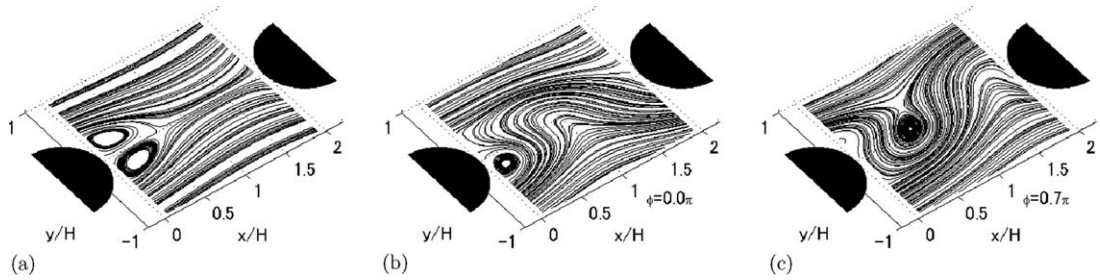

Fig. 8. Comparison of streamlines: (a) time-averaged streamline, (b) phase-averaged streamline at $\phi = 0$ and (c) phase-averaged streamline at $\phi = 0.7\pi$.

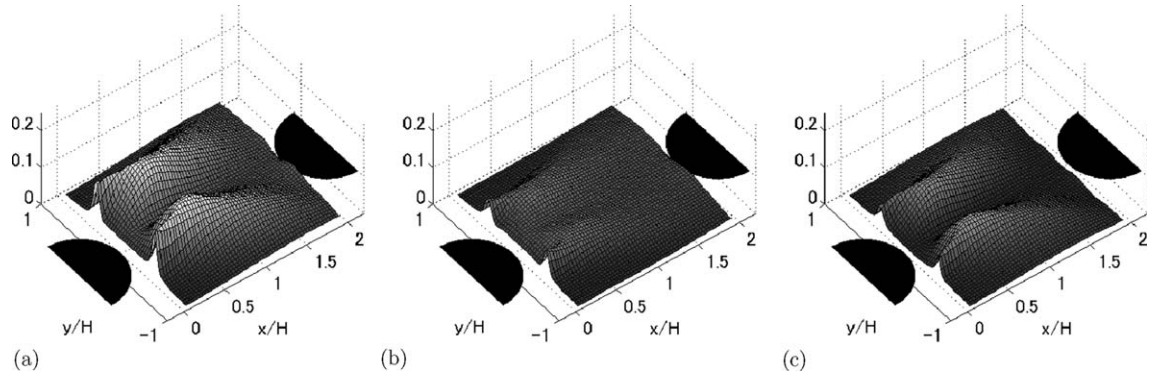

Fig. 9. Streamwise normal component of Reynolds stress: (a) $\overline{u^2}/U_c^2$ (total), (b) $\overline{u'^2}/U_c^2$ (turbulent) and (c) $\overline{\tilde{u}^2}/U_c^2$ (periodic).

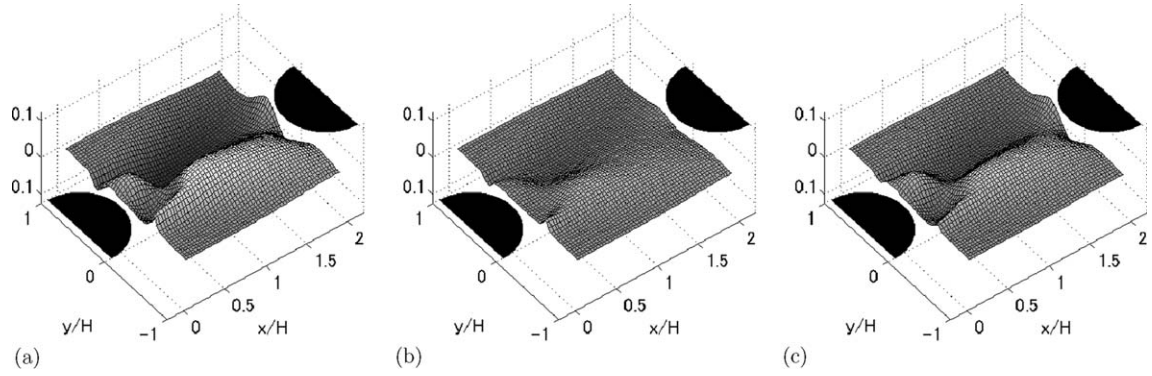

Fig. 10. Reynolds shear stress: (a) $\overline{uv}/U_c^2$ (total), (b) $\overline{u'v'}/U_c^2$ (turbulent) and (c) $\overline{\tilde{u}\tilde{v}}/U_c^2$ (periodic).

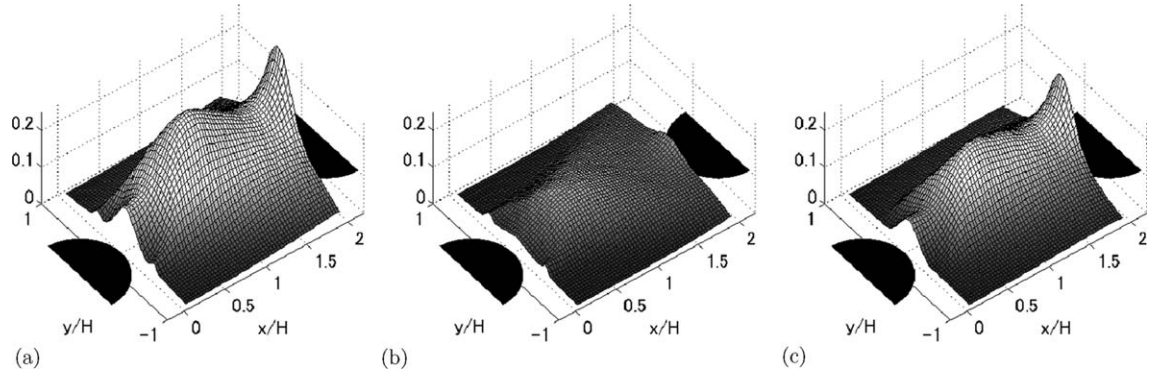

Fig. 11. Transverse normal component of Reynolds stress: (a) $\overline{v^2}/U_c^2$ (total), (b) $\overline{v'^2}/U_c^2$ (turbulent) and (c) $\overline{\tilde{v}^2}/U_c^2$ (periodic).

and periodic parts reveals the fact that the strong fluctuations are mostly due to the periodic motion, i.e., the periodic vortex shedding from the upstream body. It is interesting to note that the distribution of the turbulent part shows a pair of peaks at $x/H = 0$, the same location as those of the other components, implying that the fluctuation at this location is a consequence of the energy redistribution as it would occur in canonical shear flows. In contrast, the periodic part shows nothing common to the distribution of turbulence; the strong peak in front of the second body is considered to be a consequence of the flip–flop motion of the impinging streamline there, as inferred from Fig. 8(b) and (c).

5. Discussion

From the results presented in the preceding section, it is expected that the URANS approach predicts the present flow with reasonable accuracy because the oscillatory vortex motion may well be captured. At the same time, it is unlikely that the existing RANS provides the strong peak of $\overline{v^2}$ component in front of the downstream body. A

straightforward conclusion might be: Use the URANS instead of RANS. However, what to do when the *organized* vortex motion is not that evident, such that the spectrum of velocity fluctuation has no significant peak but only a broad distribution? In the present section, a possible modification to the models within the framework of RANS approach is discussed.

The unsatisfactory performance of the RANS models is often attributed to the existence of coherent structure in massively separated shear layer. However, once averaged over a sufficiently long time, there is no trace of coherence in the governing equation. For the improvements of RANS models, the discussions should be restricted to the terms appearing in the exact transport equation of Reynolds stresses. The most probable element that may reflect the large-scale vortex motion would be the terms containing velocity–pressure correlation, i.e., pressure diffusion and re-distribution. Here, these two terms are treated together as velocity–pressure gradient correlation.

Taking advantage of the PIV measurement, the distribution of instantaneous pressure gradient is inferred by solving discrete Poisson equation of pressure by the method described in Section 2. The results are presented in Fig. 12 for the three components of Reynolds stress under consideration

$$\Pi_{ij} = -\overline{u_i \frac{\partial p}{\partial x_j}} - \overline{u_j \frac{\partial p}{\partial x_i}}. \tag{8}$$

The role of this term may be interpreted as the composite of pressure diffusion and re-distribution of Reynolds stresses. Since the pressure diffusion does not appear in divergence form in the individual stress equation, this term does not reflect the transport of stress. Nevertheless, the comparison with the corresponding production term

$$P_{ij} = -\rho\overline{u_i u_k}\frac{\partial U_j}{\partial x_k} - \rho\overline{u_j u_k}\frac{\partial U_i}{\partial x_k}, \tag{9}$$

well explains the function of these processes. The production term of individual Reynolds stress shown in Fig. 13 points to the fact that the term Π_{ij} functions as a sink, for example, it is readily seen that P_{11} and Π_{11} show analogue distributions with opposite sign. The same is true for P_{12} and Π_{12}. However, the situation is different for the transverse normal stress component $\overline{v^2}$, namely, the production term P_{22} becomes *negative* in front of the

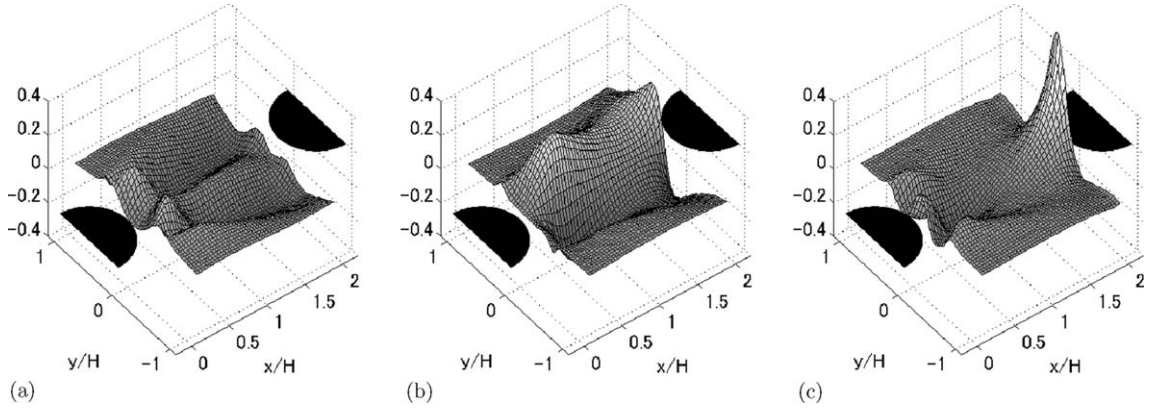

Fig. 12. Correlation of velocity and pressure gradient. (a) $\Pi_{11}/(H/\rho U_c^3)$, (b) $\Pi_{12}/(H/\rho U_c^3)$ and (c) $\Pi_{22}/(H/\rho U_c^3)$.

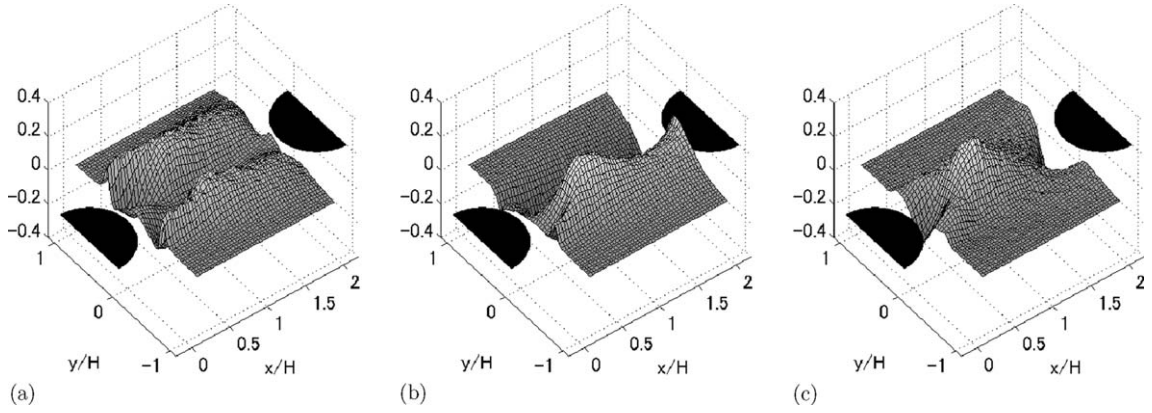

Fig. 13. Production term of total Reynolds stresses. (a) $P_{11}/(H/\rho U_c^3)$, (b) $P_{12}/(H/\rho U_c^3)$ and (c) $P_{22}/(H/\rho U_c^3)$.

downstream body where $\overline{v^2}$ shows an extreme peak. Interestingly, this peak is provided by the Π_{22} term shown in Fig. 12(c).

The negative P_{22} is a consequence of the product of the corresponding Reynolds stresses and the mean shear rates: The contents of P_{22} are

$$P_{22} = -2\overline{uv}\frac{\partial V}{\partial x} - 2\overline{v^2}\frac{\partial V}{\partial y} \tag{10}$$

and it is readily inferred from the observation of the time-averaged streamline pattern in Fig. 8(a) that the sign of the mean shear rate $\partial V/\partial y$ is always positive in front of the downstream body, and when it is multiplied by large $\overline{v^2}$, the second term in Eq. (10) becomes negative and contributes as a large sink. On the other hand, the large Π_{22} is due to a positive correlation of v and $\partial p/\partial y$. The strong fluctuating pressure gradient in front of the downstream body is caused by the flip–flop motion of the impinging streamline as illustrated in Fig. 8(b) and (c), and this oscillatory motion results in the strong correlation between the fluctuating velocity and pressure gradient as found in a similar configuration (Tokai and Obi, 2005). It is therefore understood that the excessively large Reynolds stress related to oscillatory or organized turbulent motion is a consequence of the strong correlation between the fluctuating velocity and pressure gradient.

The above observation points to the fact that the oscillatory fluid motion is represented by the velocity–pressure gradient term from the RANS point of view, which has not been considered within the conventional framework. In addition, the strong anisotropy of the normal stress components is another unusual factor, because the common algebraic relationship between Reynolds stresses cannot express such a strong anisotropy. Although any concrete modeling strategy is not known at the present, the modification of the existing RANS model for this process may improve the prediction in flows with massive separation, and if it is possible, the differential Reynolds stress model that expresses the transport of individual stress component is probably the only candidate.

6. Conclusions

The flow around a pair of bluff bodies set in tandem in uniform flow has been experimentally investigated. The three-level decomposition of the velocity data obtained by PIV has revealed that the strong turbulence intensity found between the bodies is caused by the oscillatory motion due to vortex shedding. The effect of vortex motion is recognized as a strong correlation between velocity and pressure gradient. The generally recognized poor performance of RANS models in predicting this kind of flows is attributed to the absence of such terms that represent this process.

Acknowledgements

The authors are grateful to Prof. S. Masuda, Keio University, and Dr. S. Kuroda, IHI, for invaluable discussions. The financial support for the present work has been provided by the Ministry of Education, Science, Sports and Culture, through Grant-in-Aid for Scientific Research (B), 15360100, 2004.

References

Bosch, G., Rodi, W., 1998. Simulation of vortex shedding past a square cylinder with different turbulence models. Int. J. Numer. Meth. Fluids 28, 601–616.

Hussain, A.K.M.F., Reynolds, W.C., 1970. The mechanics of an organized wave in turbulent shear flow. J. Fluid Mech. 41, 241–258.

Iaccarino, G., Ooi, A., Durbin, P.A., Behnia, M., 2003. Reynolds averaged simulation of unsteady separated flow. Int. J. Heat Fluid Flow 24, 147–156.

Kuroda, S., Sugimoto, T., Shito, M., 2003. Private communication.

Lyn, D.A., Rodi, W., 1994. The flapping shear layer formed by flow separation from the forward corner of a square cylinder. J. Fluid Mech. 267, 353–376.

Lyn, D.A., Einav, S., Rodi, W., Park, J.-H., 1995. A laser-Doppler velocimetry study of ensemble-averaged characteristics of the turbulent near wake of a square cylinder. J. Fluid Mech. 304, 285–319.

Tokai, N., Obi, S., 2005. Oscillatory turbulent flow around a pair of square cylinders in tandem, In: Proc. Int. Conf. Jets, Wakes and Separated Flows, Mie, 527–532.

Vezza, M., Taylor, I., 2003. An overview of numerical bridge deck aerodynamics. The QNET-CFD Network Newsletter 2 (2), 21–26.

Yoshioka, S., Obi, S., Masuda, S., 2001a. Organized vortex motion in periodically perturbed turbulent separated flow over a backward-facing step. Int. J. Heat Fluid Flow 22 (3), 302–307.

Yoshioka, S., Obi, S., Masuda, S., 2001b. Turbulence statistics of periodically perturbed separated flow over backward-facing step. Int. J. Heat Fluid Flow 22 (4), 393–401.

Zdravkovich, M.M., 1997. Flow around circular cylinders. Oxford University Press, Oxford, UK.